PAPER

Check for updates

Doped 2D SnS materials derived from liquid metal-solution for tunable optoelectronic devices†

Xiangyang Guo, [ID] ‡[a] Yichao Wang, [ID] ‡[a,b] Aaron Elbourne, [ID] [a] Aishani Mazumder,[a] Chung Kim Nguyen,[a] Vaishnavi Krishnamurthi, [ID] [a] Jerry Yu,[a] Peter C. Sherrell, [ID] [c] Torben Daeneke, [ID] [a] Sumeet Walia,[a] Yongxiang Li*[a] and Ali Zavabeti [ID] *[a,c]

Gas−liquid reaction phenomena on liquid-metal solvents can be used to form intriguing 2D materials with large lateral dimensions, where the free energies of formation determine the final product. A vast selection of elements can be incorporated into the liquid metal-based nanostructures, offering a versatile platform for fabricating novel optoelectronic devices. While conventional doping techniques of semiconductors present several challenges for 2D materials. Liquid metals provide a facile route for obtaining doped 2D semiconductors. In this work, we successfully demonstrate that the doping of 2D SnS can be realized in a glove box containing a diluted H_2S gas. Low melting point elements such as Bi and In are alloyed with base liquid Sn in varying concentrations, resulting in the doping of 2D SnS layers incorporating Bi and In sulphides. Optoelectronic properties for photodetectors and piezoelectronics can be fine-tuned through the controlled introduction of selective migration doping. The structural modification of 2D SnS results in a 22.6% enhancement of the d_{11} piezoelectric coefficient. In addition, photodetector response times have increased by several orders of magnitude. Doping methods using liquid metals have significantly changed the photodiode and piezoelectric device performances, providing a powerful approach to tune optoelectronic device outputs.

1. Introduction

Inspired by the intriguing properties of two-dimensional (2D) materials, significant leaps in the synthesis and engineering of nanomaterials have been made.[1,2] Several classes of 2D materials have been extensively studied; however, post-transition metal chalcogenides (PTMCs) have remained underexplored. Group IV mono-chalcogenide compounds, including SnS, SnSe, GeS, and GeSe, are typical PTMDs, showcasing promising semiconducting materials for high-performance optoelectronics,[3,4] energy,[5,6] thermoelectric,[7] and nanogenerator technology.[8] It has been previously reported that their bandgap offers optimal absorption in the solar spectrum and the piezoresponse is more than an order of magnitude in comparison to the conventionally used state-of-the-art materials.[9]

Despite the tremendous potential of PTMCs, exploiting PTMCs in practical device applications remain challenging due to the difficulty in synthesizing large area (100 μm) pinhole-free 2D layers. SnS, a representative PTMC group IV monochalcogenide has been widely employed in nanoelectronics, optoelectronics, visible-light photocatalysis, piezoelectric nanogenerator, mechanical, ferroelectric memory, and various other applications.[10–12] Synthesis of 2D SnS has been established through the liquid metal route, and their applications in piezoelectricity and photodetection have been comprehensively studied.[4,8] In particular, computational studies *via* density functional theory (DFT) have established newly formed boundary conditions for 2D SnS with a theoretical piezo-coefficient as between $d_{11} \approx 144$ pm V^{-1} (relaxed-ion) and $d_{11} \approx 22$ pm V^{-1} (clamped-ion).[8,13] These results indicate a further potential to experimentally enhance the optoelectronic properties of 2D SnS to such potentially achievable values.[13,14]

Several engineering routes to tune optoelectronics properties of 2D materials exist, including atomic substitutions, external charge transfer, insertion layer, electrostatic doping, Janus structure formations, defect engineering, zero-valent intercalation, floating gate modulation, and promoting the development of multi-functional devices.[15–20] Doping of semiconductors is one the most established modification method for building tailored modern electronic components and

[a]School of Engineering, RMIT University, Melbourne, VIC, 3000, Australia. E-mail: yongxiang.li@rmit.edu.au

[b]School of Life and Environmental Sciences, Deakin University, Geelong, Victoria, 3216, Australia

[c]Department of Chemical Engineering, The University of Melbourne, Parkville, Victoria 3010, Australia. E-mail: ali.zavabeti@unimelb.edu.au

†Electronic supplementary information (ESI) available: It contains information about process, materials characterization, photodetection an piezoelectric measurements. See DOI: https://doi.org/10.1039/d2nr01135b

‡These authors contributed equally.

devices.[21,22] SnS doping has been reported using different techniques and metals such as Bi,[23] Pb,[24,25] Cu,[26] In,[27] Sb,[28] Nd,[29] Al,[30] Fe,[31] Ce,[32] and Ag,[33] which significantly altered their structure and composition to produce desirable opto-electronic properties. However, a controllable, facile and universal doping method has not been developed for 2D SnS.

In this work, liquid metal solutions are introduced as a reaction medium for the controlled synthesis of doped 2D SnS. Low melting point metals, including Bi and In, were mixed with Sn as a base liquid metal and exposed to H_2S as a reactant gas. Uniquely, a self-limiting layer of doped 2D SnS was formed on the surface of liquid metal alloy. The 2D layers can
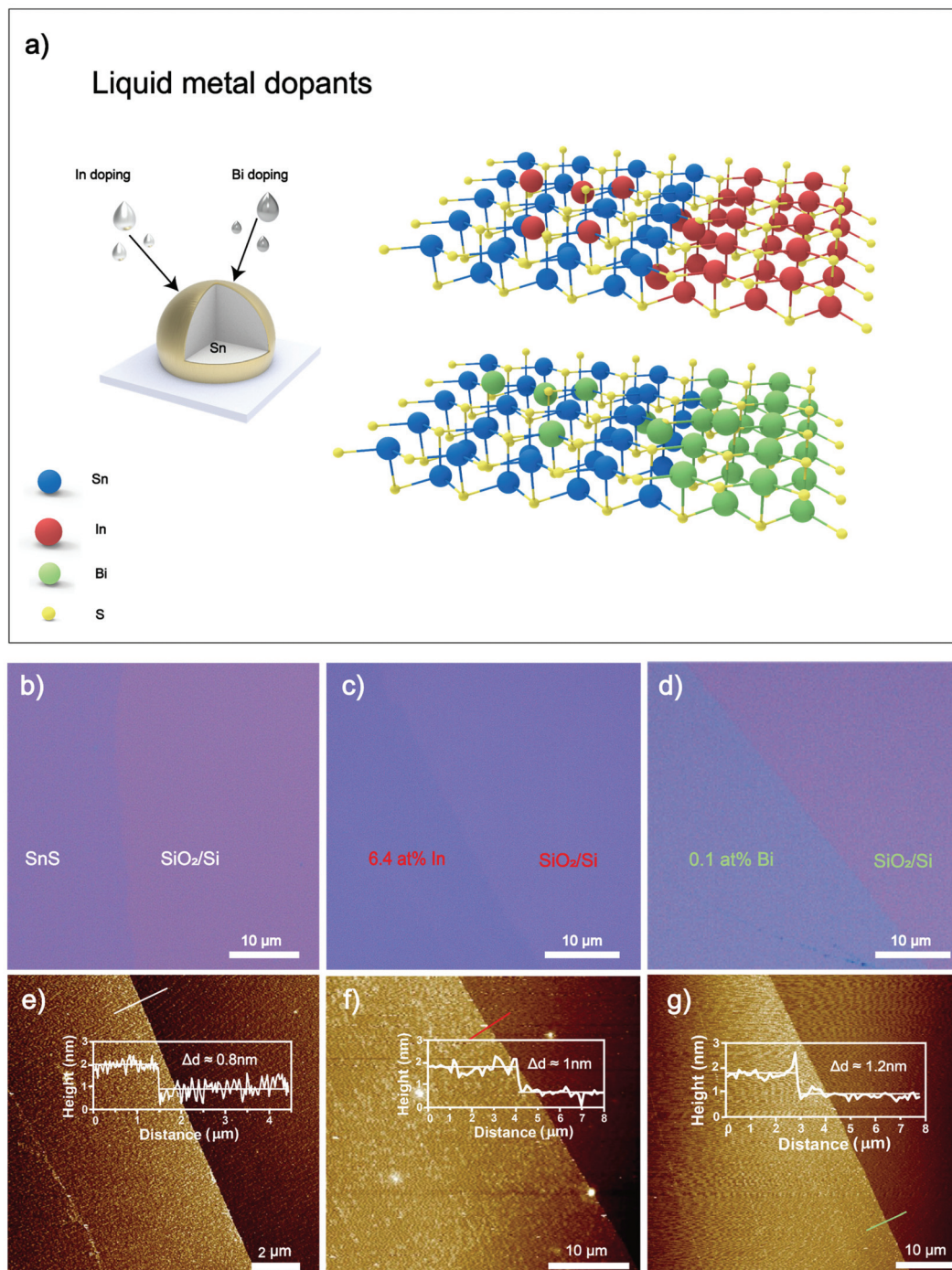
Fig. 1   (a) The schematic diagram illustrates the transfer of the 2D SnS nanosheet to the SiO₂/Si substrate by the mixed alloy (wt%) through the van der Waals touch printing method. (b–d) Optical images of undoped, 6.4 at% In and 0.1 at% Bi doped 2D SnS, respectively. The color contrast between the nanosheet and SiO₂/Si substrates can be clearly observed. (e–g) AFM topography and height profile illustrates the film thickness corresponding to b–d. The height profiles along the white (e), red (f) and green (g) lines overlaid on the images.

be transferred to a desired substrate by touching the substrate to the droplet with ease. The transferred Bi_2S_3 and In_2S_3 doped 2D SnS feature uniform, pinhole-free nanosheets with hundreds of micrometers lateral dimensions. Adjusting the liquid metal alloy concentration ratios allowed for compositional doping to produce Sn_xIn_yS and Sn_xBi_yS stoichiometries, with subsequently varied optoelectronic properties. Sn_xIn_yS with 6.4 at% Sn_xIn_yS has significantly enhanced the d_{11} piezo coefficient by ~22.6% compared to previous studies, with the piezoelectric d_{11} coefficient reaching a value as high as ~37.5 pm V^{-1}.[8] In contrast, the Sn_xBi_yS sheets showed no observable piezoelectric effect. However, the Sn_xBi_yS showed a remarkable improvement in photodetection at 0.1 at% Bi_2S_3 doping, where a substantial increase in fall times by several orders of magni-

tude was observed. Thus, this material can be used explicitly in neuromorphic applications such as artificial optoelectronic synapses and nociceptors.

2. Results and discussion

The synthesis and exfoliation of 2D SnS was performed by a liquid metal protocol that was well developed (ESI Fig. S1†).[4,8] The schematic shown in Fig. 1a represents the doping strategy to produce 2D SnS using a liquid metal alloy of Sn with Bi or In metals. The weight ratios of the alloyed metals were adjusted according to the added metal reactivity, ensuring the dominating crystal structure is that of SnS. Due to the higher

Fig. 2 (a) The Sn XPS spectra of 0.1 at% Bi doped in SnS nanosheet (Sn 3d$_{5/2}$ and Sn 3d$_{3/2}$). (b) The Bi XPS spectra of 0.1 at% Bi doped in SnS nanosheet (Bi 4f$_{7/2}$ and Bi 4f$_{5/2}$). (c) The Sn XPS spectra of 6.4 at% In doped in SnS nanosheet (Sn 3d$_{5/2}$ and Sn 3d$_{3/2}$) (d) The In^{3+} XPS spectra of 6.4 at% In doped in SnS nanosheet (In 3d$_{5/2}$ and In 3d$_{5/2}$). (e) Quantitative measurement of 2D doped Bi^{3+} (0, 0.1, 0.4 and 0.6 at%) obtained from alloys mixed with different weight ratios of 25, 50, 75 and 90 wt% from left to right. The error bars represent the standard errors of the doping ratios of four different measurements. (f) Quantitative measurement of the 2D doping of In^{3+} (2.4, 6.4, 11 and 17 at%) obtained from alloys mixed with different weight ratios of 0.1, 0.3, 0.6 and 0.9 wt%. The error bars represent the standard errors of the doping ratios of four different measurements.

reactivity of In than Sn,[34] less than 0.9 wt% In : Sn ratios were investigated. In contrast, Bi is less reactive than Sn; hence, alloy concentrations of more than 25 wt% Bi : Sn ratios were explored. Various weight ratios of alloyed metals were prepared, firstly for In : Sn of 0.1, 0.3, 0.6 and 0.9 wt% and secondly, Bi : Sn ratios of 25, 50, 75 and 90 wt%. Metal chunks were transferred to a glove box purged with N_2, melted at ~300 °C, and mixed with a glass rod. The alloy is separated into smaller pellets to be used during synthesis. Before starting the experiment, the glovebox was purged with N_2 with a flow rate of 500 sccm for 2 h, and then the gas flow controller was changed to 50 ppm H_2S (in Argon). The prepared alloy pellet was placed on a glass slide and heated to 350 °C by a ceramic heating plate. The formed 2D SnS layers adhere weakly to the liquid metal surface, and a van der Waals touch transfer can isolate 2D layers onto the desired substrate with ease.[4]

Large area (i.e., hundreds of micrometers), doped 2D SnS nanosheets were then obtained by van der Waals transfer to the substrate. Optical images in Fig. 1b–d elucidate the smooth and uniform transferred 2D sheets of the pristine, In and Bi-doped SnS onto the SiO_2/Si substrates, respectively. Atomic force microscopy (AFM) is used to characterize the thickness of the transferred 2D nanosheets. The thickness of pristine 2D SnS nanosheets is measured as 0.8 nm (Fig. 1e). In doped 2D sheets were measured to be 1.0 nm thick (Fig. 1f), and Bi doped 2D sheets were measured at 1.2 nm thick (Fig. 1g), correlating to the greater atom size of In and Bi respectively.

X-ray photoelectron spectroscopy (XPS) is used to analyze the atomic composition of doped 2D SnS (Fig. 2a–d, ESI Fig. S2 and S3†). The XPS results in Fig. 2b show the binding energies of Bi cations and the Bi $4f_{7/2}$ peak is located at 158.5 eV and Bi $4f_{5/2}$ peak is located at 163.7 eV.[35] The In-doped sample in Fig. 2d shows the In $3d_{5/2}$ peak situated at 444.8 eV and the In $3d_{3/2}$ peak which is situated at 452.4 eV.[36] No metallic state of the Bi and In was observed in the printed 2D SnS, suggesting the existence of these atoms in the crystal structure as the cations. The Sn $3d_{5/2}$ peak of Sn in 2D SnS is located at 486.5 eV and Sn $3d_{3/2}$ peak is located at 494.9 eV, representing the oxidation state of SnS.[4,8] The Bi : Sn alloy concentration was incrementally changed from 25, 50, 75 to 90 wt%, where the 90% Bi : Sn alloy had the highest Bi-doping concentration of 0.6 at% in the 2D nanosheets. In comparison, as the In : Sn alloy concentration ratio increased, from 0.1, 0.3, 0.6, to 0.9 wt%, the In-doping significantly increased to 17 at% 2D nanosheets from the In : Sn alloy of 0.9 wt%. The detailed XPS analysis results are presented in the ESI Fig. S2 and S3.†

High-resolution transmission electron microscopy (HRTEM) was used to analyze crystal structure and atomic spacings (Fig. 3). 2D samples were printed directly on holey carbon grids. Doping had resulted in the generation of grain boundaries of In_2S_3 and Bi_2S_3 as shown in Fig. 3e and f. Interestingly, the boundaries are connected through an interface between 2D SnS and In_2S_3 and Bi_2S_3 grains that are void from breakages and damage, confirming a smooth 2D formation observed from optical and AFM measurements as seen in Fig. 1. The sulphide crystal structure for In_2S_3 and Bi_2S_3 are consistent with previously reported liquid metal obtained 2D sulphides.[37,38]

The optoelectronic properties of pristine 2D SnS has been demonstrated, showing ultrafast photodetection responses of 22 μs.[4] The photoresponse measurement of Bi-doped 2D SnS was performed at room temperature by irradiating monochro-

Fig. 3 (a–c) The bright-field TEM image of undoped 2D SnS and 6.4 at% In and 0.1% Bi doped 2D SnS, respectively. (d–e) HRTEM images of the corresponding TEM images in a–c showing the formation of In_2S_3 and Bi_2S_3 grains. The sulfide doping formation is in agreement with the oxide counterpart.[22]

matic light on a device with a 100 μm active area (Fig. 4a and b). Fig. 4c shows the variation of the photocurrent D_{Iph} (D_{Iph} = $I_{Illumination} - I_{dark}$) with different wavelengths when the illumination power density is 2 mW cm^{-2} under a 0.5 V applied bias. The D_{Iph} value is the highest at 365 nm. It can be observed that light with a wavelength of 365 nm has the strongest effect on the generation of photoexcited carriers. With an increase of wavelength, the energy of light decreases, so the generation of photoexcited carriers also decreases at 1050 nm. Fig. 4d shows the rise and fall times under the irradiation of the wavelength that produces the most photoactive carriers. For the 365 nm wavelength irradiation, the rise time is about 1.9 s. This rise time is significantly longer than that of the previous experiment by Krishnamurthi *et al.* (ESI Fig. S4†),[4] where the rise time of the 2D SnS film is ~22 μs.

Similarly, the fall time of this experiment is 9.6–189.4 s, which is much longer than the fall time of the undoped 2D SnS film of 51 μs.[4] The experimental results reveal a slow rise and decay which can be associated with grain boundary gene-

ration. Fig. 4e mainly shows D_{Iph} relative to the baseline under the excitation of different wavelengths of light. It can be clearly observed that the 365 nm wavelength light changes the photocurrent D_{Iph} the most, which is close to 92%. With the wavelength increasing, the change amplitude of the photocurrent D_{Iph} decreases correspondingly. The rate of decrease at 565 nm and 660 nm consequently maintains a change of 25% and finally drops to about 5% at 1050 nm wavelength light. The results of such photodetectors are substantially different from Krishnamurthi *et al.*[4] The photocurrent generation has longer fall times from non-doped of 22 μs (ref. 4) to Bi-doped of 189.4 s (Fig. 4d and ESI Fig. S4a†). The long exciton lifetime is due to crystal grain formations leading to increased exciton trappings, augmenting the relaxation pathways. This phenomenon has been reported in doped tin sulfide compounds using Na,[39] In,[40] Sb[28] and Al.[41]

Group IV monochalcogenides (MX, M – Sn or Ge, X – Se or S), namely SnSe, SnS, GeSe and GeS, has recently become an emerging area for piezoelectric research featuring stable non-

Fig. 4 (a) Schematic diagram of the optoelectronic performance device. (b) Photocurrent at different wavelengths for a single layer of 0.1 at% Bi doping SnS. (c) Photocurrent (D_{Iph}) of different monochromatic lights with different wavelengths in the static voltage bias from −0.5 V to +0.5 V, including dark conditions. (d) The response time of 0.1 at% Bi-doped 2d SnS nanosheet at a wavelength of 285 nm and a frequency of 500 Hz measured between 10% and 90% of the step height. (e) The photocurrent changes by ratio obtained at different wavelengths at P_{inc} = 2 mW cm^{-2} and V_{ds} = 0.5 V for a single layer of 0.1 at% Bi-doped in SnS nanosheet.

Fig. 5 2D SnS with 6.4 at% In doping lateral piezoelectric response. (a) The AFM morphology and the 2D layer. (b) 6.4 at% In alloy concentration single layer Lateral amplitude, histogram with the attached picture. (c) 6.4 at% In doped in SnS lateral phase, the inset is a histogram. (d) The lateral piezoelectric response of 6.4 at% In doped in SnS single layer nano-film, pristine and PPLN to different driving voltages. Error bars indicate the standard deviation of the measurement.

centrosymmetric crystals.[42] Secondly, their puckered C_{2v} symmetry is more flexible (softer) in the armchair direction, further enhancing the piezoelectric effect.[43] 2D SnS nanosheets have been simulated by first-principles density functional theory (DFT) to calculate the piezoelectric coefficients. The d_{11} coefficient has been calculated to be two orders of magnitude larger than those of other 2D materials and bulk materials.[14] Fig. 5a shows the morphology of the synthesized 2D SnS with a thickness of ~1 nm. Fig. 5b, c and ESI Fig. S5† show the results of the lateral piezoelectric effect and phase of the In-doped 2D SnS. For benchmarking, the comparison of In-doped and pristine 2D SnS and periodically polarized lithium niobate (PPLN) reference sample with the lateral piezoelectric response are shown in Fig. 5d. The results of these three samples show that with the increase of the driving voltage, the piezoelectric response illustrates a linear increase. The slope of the linear fitting line can be used to calculate the effective piezoelectric coefficient. The doped and pristine 2D SnS and the reference PPLN sample have relative slopes of $1:0.6:0.16$, respectively. Since the lateral direction of PPLN $d_{\mathrm{eff}} = 5.92$ pm V^{-1} (ESI Fig. S6†), the In-doped single-layer SnS can be calculated, the effective piezoelectric coefficient is

37.5 pm V^{-1}. Khan *et al.* found the piezoelectric response of pristine 2D SnS as is 26 pm V^{-1}.[8] Compared with pristine (ESI Fig. S7†), the piezoelectric response of In-doped 2D SnS is remarkably increased by ~22.6%. However, in contrast, Bi doping has quenched the piezoresponse of the material (ESI Fig. S5 and S8†). This quenched response demonstrates clearly that there is negligible substrate effect and no artifacts from contact electrification in the PFM data.[44] It is thought that the large atom size of Bi should increase asymmetry in the SnS crystal structure, so further studies and theoretical interpretation are needed to understand why there is zero piezoelectric response.

3. Conclusions

Engineering 2D materials is a promising pathway to fully exploit their potential. Liquid metals offer a novel platform for obtaining unique 2D materials and enable the manipulation of 2D compositions. In this work, liquid metal methods are used to dope 2D SnS based on the selective migration mechanism.[22] We selected Bi and In due to the potential formation

of substitutional alloy and the low melting point of the base metals. For comparing Gibbs free energy (ΔG_f) of reaction for the formation of In_2S_3, SnS and Bi_2S_3 the normalized energy based on the unit-mole of the reactant was calculated. The normalized energies were −165, −98.3 and −56.24 (kJ mol^{-1}) respectively.[45] The more negative ΔG_f represents the higher reactivity. Therefore the metal dopants have been selected accordingly so that the 2D sheets are dominated by SnS.

The liquid metal doping of In in 2D SnS has shown a substantial 22.6% increase in piezoelectric coefficient achieved at 6.4 at% In : Sn. This is due to the doping effect on augmenting the polarization. In addition, broadband photodetection performance of doped SnS was analyzed. The high-energy photon wavelength of 365 nm excites the maximum number of electrons located in the valence band to the high-energy conduction band allowing the practical analysis of the response times. The response time is affected by carrier transition time during the recombination, in which several defects and consequently spacially isolated potential barriers prolong the recombination equilibrium. The response time was increased by several orders rendering a significant carrier lifetime compared with the pristine 2D SnS, which can aid in realising applications for neuromorphics. These results suggest a vast opportunity for tuning and engineering 2D nanosheets for optoelectronics performances using the liquid metal approach.

4. Experimental

4.1. Materials

Tin (Sn, 99.8%), bismuth (Bi, 99.98%) and indium (In, 99.99%) were purchased from Roto Metals. All other reagents and solvents were obtained from Sigma-Aldrich and used according to the received standards.

4.2. Liquid metal alloy preparation

One-step touch printing uses van der Waals force to exfoliate the doped 2D SnS film. Firstly, the pre-alloy is obtained by configuring different weight ratios of Bi/Sn and In/Sn. The weight ratios of Bi/Sn of the alloy are 25 wt%, 50 wt%, 75 wt% and 90%, and the weight ratios of In/Sn of the alloy are 0.1%, 0.3%, 0.6% and 0.9%, respectively. After these alloys are weighed by a digital scale, they are transferred to a glove box filled with N_2. The O_2 concentration in the glove box is strictly controlled. These mixed metals are placed in a glass bottle. Through the heating plate in the glove box, these metals were heated over 300 °C and thoroughly mixed, and then the bottle is removed from the heating plate and cooled naturally to a solid, ready for the next reaction in the H_2S environment.

The touch printing of doping 2D SnS nanosheet is carried out in a small glove box. In order to exhaust all O_2 gas in the chamber, N_2 with a flow rate of 500 sccm is pumped into the chamber for more than two hours and then switched to 50 ppm of H_2S gas, which is pumped into the chamber at a flow rate of 500 sccm for an hour, so that the small glove box

is filled with H_2S gas. The pre-mixed alloy is placed on a glass slide, and the glass slide is heated to 350 °C, at this time, the solid metal has melted into a shiny metal ball, but the surface of the silver-white metal ball will gradually turn yellow-brown in the H_2S atmosphere, which means that the SnS layer has been formed. At this time, the pre-heated SiO_2/Si substrate is ready for printing.

4.3. 2D characterization

The optical image is obtained by using Leica DM2500 optical microscope to observe the In and Bi doped SnS nanosheets on 300 nm SiO_2/Si substrates, and the surface morphology image is measured by a Bruker Dimension Icon atomic force microscope (AFM) in ScanAsyst-air mode, and Gwyddion 2.55 software is used to analyze the thickness distribution and surface morphology of 2D nanosheets. The crystal phase analysis is carried out by using JEOL JEM-2100F microscope operating at 200 kV acceleration voltage to obtain low/high-resolution TEM imaging and selected area electron diffraction images. The 2D nanosheets are transferred to the substrate by touch printing with holey Au–Carbon grids (ProScitech, Australia). The analysis of elemental composition is performed using Thermo Scientific K-alpha XPS spectrometer with 1486.7 eV (Al Kα) X-ray source. The CasaXPS software is used for data analyses.

4.4. Piezoresponse force microscopy

The characteristics of piezoelectric properties are measured using MFP-Infinity (Oxford Instrument, Asylum Research, Santa Barbara, CA, USA) equipment in the lateral piezoresponse force microscopy (LPFM) mode. The sample chip is interfaced on the magnetic metal piece with double-sided tape, and put the sample with the magnetic metal piece on the metal base together. In order to ensure the accuracy of the piezoelectric results, we pre-measured Asylum Research periodically polarized lithium niobate (AR-PPLN) standard samples to calculate the piezoelectric coefficient d_{eff} of the PPLN, so it can be calibrated with the known coefficient pristine and In-doped SnS.

4.5. Device fabrication and measurement

The 2D SnS nanosheet is transferred to a 300 nm SiO_2/conductive silicon substrate, and then coated with AZ-5214E photoresist. The designed interdigital electrode is patterned by a maskless aligner – Heildberg MLA150, and the AZ-726 MIF Developer is used to flush the pattern scanned by the laser. The PVD75 Kurt J. Lesker electron beam evaporator is used to deposit Cr/Au (10/100 nm) electrodes on the 2D nanosheet. For photoelectric measurement, a commercial monochromatic light emitting diode (Thorlabs, Inc.) is used as the excitation source with a wavelength range of 280–1050 nm. All measurements are carried under dark ambient environment. Illumination power is calibrated by UV-enhanced photodetectors (Newport Corporation). The laser is irradiated on the nanosheet from top to bottom, and the power intensity is fixed at 2 mW cm^{-2} for varies wavelengths ranging between 280 nm to 1050 nm.

Author contributions

X. G., Y. W., J. Y., Y. L. and A. Z. conceptualized the project; X. G., Y. W., and A. E. performed piezoelectric measurements; X. G., A. M. performed photodetection characterizations; C. K. N. conducted UV-Vis measurements, X. G. and V. K. performed materials synthesis and device fabrication; X. G., Y. W. and Y. L. performed materials characterizations; and validation; All other authors have contributed to writing, review & editing; Y. L. and A. Z. performed supervision.

Conflicts of interest

There are no conflicts to declare.

Acknowledgements

References

1 R. Mas-Balleste, C. Gomez-Navarro, J. Gomez-Herrero and F. Zamora, *Nanoscale*, 2011, **3**, 20–30.

2 K. Khan, A. K. Tareen, M. Aslam, R. Wang, Y. Zhang, A. Mahmood, Z. Ouyang, H. Zhang and Z. Guo, *J. Mater. Chem. C*, 2020, **8**, 387–440.

3 B. Mukherjee, Y. Cai, H. R. Tan, Y. P. Feng, E. S. Tok and C. H. Sow, *ACS Appl. Mater. Interfaces*, 2013, **5**, 9594–9604.

4 V. Krishnamurthi, H. Khan, T. Ahmed, A. Zavabeti, S. A. Tawfik, S. K. Jain, M. J. S. Spencer, S. Balendhran, K. B. Crozier, Z. Li, L. Fu, M. Mohiuddin, M. X. Low, B. Shabbir, A. Boes, A. Mitchell, C. F. McConville, Y. Li, K. Kalantar-Zadeh, N. Mahmood and S. Walia, *Adv. Mater.*, 2020, **32**, e2004247.

5 J. Lu, C. Nan, L. Li, Q. Peng and Y. Li, *Nano Res.*, 2012, **6**, 55–64.

6 C. Zhang, H. Yin, M. Han, Z. Dai, H. Pang, Y. Zheng, Y.-Q. Lan, J. Bao and J. Zhu, *ACS Nano*, 2014, **8**, 3761–3770.

7 L. D. Zhao, S. H. Lo, Y. Zhang, H. Sun, G. Tan, C. Uher, C. Wolverton, V. P. Dravid and M. G. Kanatzidis, *Nature*, 2014, **508**, 373–377.

8 H. Khan, N. Mahmood, A. Zavabeti, A. Elbourne, M. A. Rahman, B. Y. Zhang, V. Krishnamurthi, P. Atkin, M. B. Ghasemian, J. Yang, G. Zheng, A. R. Ravindran, S. Walia, L. Wang, S. P. Russo, T. Daeneke, Y. Li and K. Kalantar-Zadeh, *Nat. Commun.*, 2020, **11**, 3449.

9 Y. Guo, S. Zhou, Y. Bai and J. Zhao, *ACS Appl. Mater. Interfaces*, 2017, **9**, 12013–12020.

10 H. Wang and X. Qian, *2D Mater.*, 2017, **4**(1), 015042.

11 J. R. Brent, D. J. Lewis, T. Lorenz, E. A. Lewis, N. Savjani, S. J. Haigh, G. Seifert, B. Derby and P. O'Brien, *J. Am. Chem. Soc.*, 2015, **137**, 12689–12696.

12 C. Xin, J. Zheng, Y. Su, S. Li, B. Zhang, Y. Feng and F. Pan, *J. Phys. Chem. C*, 2016, **120**, 22663–22669.

13 L. C. Gomes, A. Carvalho and A. H. Castro Neto, *Phys. Rev. B: Condens. Matter Mater. Phys.*, 2015, **92**(21), 214103.

14 R. Fei, W. Li, J. Li and L. Yang, *Appl. Phys. Lett.*, 2015, **10**(17), 173104.

15 P. Luo, F. Zhuge, Q. Zhang, Y. Chen, L. Lv, Y. Huang, H. Li and T. Zhai, *Nanoscale Horiz.*, 2019, **4**, 26–51.

16 Z. Hu, Z. Wu, C. Han, J. He, Z. Ni and W. Chen, *Chem. Soc. Rev.*, 2018, **47**, 3100–3128.

17 W. Liao, S. Zhao, F. Li, C. Wang, Y. Ge, H. Wang, S. Wang and H. Zhang, *Nanoscale Horiz.*, 2020, **5**, 787–807.

18 W. Shin, S. Hong, Y. Jeong, G. Jung, J. Park, D. Kim, C. Lee, B. G. Park and J. H. Lee, *Nanoscale*, 2021, **13**, 9009–9017.

19 V. Van On, D. K. Nguyen, J. Guerrero-Sanchez and D. M. Hoat, *New J. Chem.*, 2021, **45**, 20776–20786.

20 Z. Wang, H. Kannan, T. Su, J. Swaminathan, S. N. Shirodkar, F. C. Robles Hernandez, H. C. Benavides, R. Vajtai, B. I. Yakobson, A. Meiyazhagan and P. M. Ajayan, *Nanoscale Adv.*, 2021, **3**, 1747–1757.

21 Y. Gong, H. Yuan, C. L. Wu, P. Tang, S. Z. Yang, A. Yang, G. Li, B. Liu, J. van de Groep, M. L. Brongersma, M. F. Chisholm, S. C. Zhang, W. Zhou and Y. Cui, *Nat. Nanotechnol.*, 2018, **13**, 294–299.

22 M. B. Ghasemian, A. Zavabeti, M. Mousavi, B. J. Murdoch, A. J. Christofferson, N. Meftahi, J. Tang, J. Han, R. Jalili, F. M. Allioux, M. Mayyas, Z. Chen, A. Elbourne, C. F. McConville, S. P. Russo, S. Ringer and K. Kalantar-Zadeh, *Adv. Mater.*, 2021, **33**, e2104793.

23 A. Dussan, F. Mesa and G. Gordillo, *J. Mater. Sci.*, 2010, **45**, 2403–2407.

24 K. Norton, J. Kunstmann, L. Ping, A. Rakowski, C. Wang, A. J. Marsden, G. Murtaza, N. Zeng, S. G. McAdams, S. J. McAdams, M. A. Bissett, S. J. Haigh, B. Derby, G. Seifert, J. C. Ke and D. J. Lewis, *Chem. Sci.*, 2019, **10**, 1035–1045.

25 F. Y. Ran, Z. Xiao, Y. Toda, H. Hiramatsu, H. Hosono and T. Kamiya, *Sci. Rep.*, 2015, **5**, 10428.

26 M. Patel and A. Ray, *RSC Adv.*, 2014, **4**, 39343–39350.

27 H. Kafashan, *Mater. Res. Express*, 2018, **5**(4), 046417.

28 M. Seal, N. Singh, E. W. McFarland and J. Baltrusaitis, *J. Phys. Chem. C*, 2015, **119**, 6471–6480.

29 S. Sebastian, I. Kulandaisamy, A. M. S. Arulanantham, S. Valanarasu, A. Kathalingam, M. Shkir and S. AlFaify, *Rare Met.*, 2022, **41**, 1661–1670.

30 S. Zhang, S. Cheng, H. Jia and H. Zhou, *Adv. Mater. Res.*, 2011, **418–420**, 712–716.

31 S. Sebastian, I. Kulandaisamy, S. Valanarasu, N. Soundaram, K. Paulraj, D. Vikraman and H.-S. Kim, *J. Mater. Sci.: Mater. Electron.*, 2019, **30**, 8024–8034.

32 Z. Wang, L. Huang, C. Zhang, M. Chuai, X. Zhang and M. Zhang, *J. Alloys Compd.*, 2019, **799**, 425–432.

33 S. Sebastian, S. Vinoth, K. H. Prasad, M. S. Revathy, S. Gobalakrishnan, P. K. Praseetha, V. Ganesh and S. AlFaify, *Appl. Phys. A*, 2020, **126**(10), 1–12.

34 A. Zavabeti, J. Z. Ou, B. J. Carey, N. Syed, R. Orrell-Trigg, E. L. H. Mayes, C. Xu, O. Kavehei, A. P. O'Mullane, R. B. Kaner, K. Kalantar-zadeh and T. Daeneke, *Science*, 2017, **358**, 332–335.

35 T. J. Whittles, L. A. Burton, J. M. Skelton, A. Walsh, T. D. Veal and V. R. Dhanak, *Chem. Mater.*, 2016, **28**, 3718–3726.

36 L. A. H. Jones, W. M. Linhart, N. Fleck, J. E. N. Swallow, P. A. E. Murgatroyd, H. Shiel, T. J. Featherstone, M. J. Smiles, P. K. Thakur, T.-L. Lee, L. J. Hardwick, J. Alaria, F. Jäckel, R. Kudrawiec, L. A. Burton, A. Walsh, J. M. Skelton, T. D. Veal and V. R. Dhanak, *Phys. Rev. Mater.*, 2020, **4**(7), 074602.

37 A. Jannat, Q. Yao, A. Zavabeti, N. Syed, B. Y. Zhang, T. Ahmed, S. Kuriakose, M. Mohiuddin, N. Pillai, F. Haque, G. Ren, D. M. Zhu, N. Cheng, Y. Du, S. A. Tawfik, M. J. S. Spencer, B. J. Murdoch, L. Wang, C. F. McConville, S. Walia, T. Daeneke, L. Zhu and J. Z. Ou, *Mater. Horiz.*, 2020, **7**, 827–834.

38 K. A. Messalea, A. Zavabeti, M. Mohiuddin, N. Syed, A. Jannat, P. Atkin, T. Ahmed, S. Walia, C. F. McConville, K. Kalantar-Zadeh, N. Mahmood, K. Khoshmanesh and T. Daeneke, *Adv. Mater. Interfaces*, 2020, **7**(22), 2001131.

39 B. Ouyang, W. He, L. Wu, L.-D. Zhao and Y. Yang, *Nano Energy*, 2021, **88**, 106268.

40 C. Fan, Z. Liu, S. Yuan, X. Meng, X. An, Y. Jing, C. Sun, Y. Zhang, Z. Zhang, M. Wang, H. Zheng and E. Li, *ACS Appl. Mater. Interfaces*, 2021, **13**, 35889–35896.

41 X. Meng, C. Fan, X. An, S. Yuan, Y. Jing, Z. Liu, C. Sun, Y. Zhang, Z. Zhang, M. Wang, H. Zheng and E. Li, *CrystEngComm*, 2021, **23**, 4694–4699.

42 P. C. Sherrell, M. Fronzi, N. A. Shepelin, A. Corletto, D. A. Winkler, M. Ford, J. G. Shapter and A. V. Ellis, *Chem. Soc. Rev.*, 2022, **51**, 650–671.

43 L. Li, Z. Chen, Y. Hu, X. Wang, T. Zhang, W. Chen and Q. Wang, *J. Am. Chem. Soc.*, 2013, **135**, 1213–1216.

44 A. Sutka, P. C. Sherrell, N. A. Shepelin, L. Lapcinskis, K. Malnieks and A. V. Ellis, *Adv. Mater.*, 2020, **32**, e2002979.

45 W. M. Haynes, *Crc Handbook of Chemistry and Physics*, CRC Press LLC, Milton, United Kingdom, 2016.